Rare Metal Materials and Engineering
Volume 50, Issue 6, June 2021
Available online at www.rmme.ac.cn

Science Press

Cite this article as: Wang Panpan, Jiang Haitao, Wang Yujiao, et al. Improvement of Hot Workability and Corrosion Resistance of Mg-3Al-1Zn-0.1Mn-0.2Ca Alloy Through Hot Deformation[J]. Rare Metal Materials and Engineering, 2021, 50(06): 1910-1918.

ARTICLE

Improvement of Hot Workability and Corrosion Resistance of Mg-3Al-1Zn-0.1Mn-0.2Ca Alloy Through Hot Deformation

Wang Panpan, Jiang Haitao, Wang Yujiao, Zhang Yun, Yu Bowen, Cao Zhiming, Zhong Binbin

Institute of Engineering Technology, University of Science and Technology Beijing, Beijing 100086, China

Abstract: The effect of efficiency of power dissipation on hot workability and corrosion behavior of AZ31 alloy was investigated. The results indicate that minor Ca-addition can significantly improve the hot workability and corrosion resistance due to grain refinement by facilitating recrystallization and formation of a more protective corrosion product layer doped with a trace amount of $Ca(OH)_2$. The instability zone exhibits worse corrosion resistance than dynamic recrystallization (DRX) domain due to heterogeneous microstructure and obvious wedge cracks. Moreover, wedge cracks caused by flow localization band can serve as channels for the diffusion of aggressive Cl^- and accelerate further corrosion of Mg matrix. The DRX domain with homogeneous fine grain microstructure and high efficiency of power dissipation obtained by hot deformation at 400 ℃/0.001 s^{-1} of Mg-Al-Zn-Mn-Ca alloy simultaneously performs superior corrosion resistance and good hot workability.

Key words: AZ31 alloy; microstructural evolution; corrosion behavior; hot workability

As we all know, the poor corrosion resistance and formability of magnesium alloy is still a great challenge to its full implementation[1]. Alloy design can modify the microstructure of the alloys and then improve the mechanical and corrosion performance simultaneously, just by incorporating specific amounts of alloying elements, such as calcium[2,3]. Chaudry et al[4,5] found that AZ31 alloy exhibits high formability due to high activity of prismatic slip and weak basal texture by Ca-addition. And the positive effect of Ca on the corrosion resistance is related to the refinement of the microstructure, the formation of a denser corrosion film layer and the increase of the β-phase area fraction which improves the barrier effect of the latter[6,7].

Fine grain microstructure of AZ31 alloy can also be obtained by conventional hot working process, such as hot deformation. And deformation conditions are very crucial to the control of microstructure regulation[8]. Tsao et al[9] indicated that the corrosion resistance of AZ61 compressed alloys is gradually improved with decreasing the temperature from 773 K to 623 K due to grain refinement. Kaviani et al[10] proposed that homogeneous fine grain microstructure by hot deformation at 400 ℃/0.001 s^{-1} for Mg-Zn-Ca-Mn alloy can simultaneously improve mechanical properties and corrosion resistance. Uniform fine-grained structure with higher efficiency of power dissipation by hot deformation at 350 ℃/0.01/10 s^{-1} of TZA822 alloy exhibits superior hot workability[11]. Wang et al concluded that the domains of 630~670 K and 0.01~1 s^{-1} with high power dissipation perform good hot workability due to a higher fraction of dynamic recrystallization (DRX) grains at high Z value[12]. However, the effect of efficiency of power dissipation on corrosion behavior of Mg alloys during hot deformation is still lack of research.

In conclusion, Ca element and hot deformation process play significant roles in hot workability and corrosion behavior. But the effect of efficiency of power dissipation on both hot workability and corrosion behavior is still unclear. Thus, this study aims to simultaneously improve the hot workability and corrosion resistance of AZ31 alloy, and elucidate the following issues: (1) microstructure evolution after hot deformation and its corrosion behavior; (2) effect of efficiency of power dissipation (η) on hot workability and corrosion behavior.

Received date: June 26, 2020
Foundation item: Fundamental Research Funds for the Central Universities (2302017FRF-IC-17-001, 2302018FRF-IC-18-004, 232019FRF-IC-19-018)
Corresponding author: Jiang Haitao, Ph. D., Professor, Institute of Engineering Technology, University of Science and Technology Beijing, Beijing 100086, P. R. China, Tel: 0086-10-62332598, E-mail: jianght@ustb.edu.cn

Copyright © 2021, Northwest Institute for Nonferrous Metal Research. Published by Science Press. All rights reserved.

1 Experiment

The alloy ingots with nominal composition of Mg-3Al-Zn-0.1Mn (abbreviated as AZ31) and Mg-3Al-Zn-0.1Mn-0.2Ca (abbreviated as AZ31-0.2Ca) were prepared by melting high purity Mg, Al and Zn (>99.99%), Mg-10wt% Mn, and Mg-20wt% Ca master alloys in the electrical resistance furnace under the protection of Ar atmosphere, and then cast into ingots with dimension of Φ130 mm×200 mm. The actual compositions of the studied alloys, as measured by inductively coupled plasma atomic emission spectrometry, are listed in Table 1. The ingots were solution-treated at 450 ℃ for 12 h, and then air-cooled. Cylindrical compression samples with the dimensions of Φ10 mm×15 mm were machined from the solution-treated AZ31 and AZ31-0.2Ca ingots. Isothermal uniaxial hot compression tests were conducted using a Gleeble 3500 thermal-mechanical simulation testing system. The samples were heated to the deformation temperature with a heating rate of 5 ℃/s and held at the deformation temperature for 3 min to ensure a uniform temperature distribution, followed by deformation and water quenching. The samples were deformed to a final true strain of 0.92 at the temperatures of 300, 350, 400, 450 ℃ with the strain rates of 0.001, 0.01, 0.1 and 1.0 s^{-1}.

The electrochemical measurement, immersion test and hydrogen evolution were all carried out in 3.5wt% NaCl solution at ambient temperature. The area of the samples in the experiment was 0.785 cm^2 (Φ10 mm×2 mm). The electrochemical measurement experiments were conducted with a typical three-electrode cell, where the specimen was working electrode, saturated calomel electrode was reference electrode and platinum was the counter electrode. The electrochemical impedance spectrometry (EIS) was recorded in the frequency range of 100 kHz to 0.01 Hz with a perturbation amplitude of 5 mV after immersing for 30 min to get the steady state potential. Polarization tests were then conducted at a scan rate of 1 mV/SCE s^{-1} in the range of ±300 mV/SCE. The E_{corr} and I_{corr} were obtained by Tafel's cathodic linear curve portion extrapolation technique.

Table 1 Composition of samples tested herein (wt%)

Alloy	Al	Zn	Mn	Ca	Mg
AZ31	3.04	0.97	0.13	-	Bal.
AZ31-0.2Ca	3.08	0.96	0.10	0.24	Bal.

The microstructure of the samples after deformation was studied along the compression axis at the mid-plane position, using a standard metallographic procedure followed by etching using a solution of 5 g picric acid, 10 mL acetic acid, 10 mL water, and 100 mL ethanol. The microstructure and corrosion morphologies were observed by ZEISS SUPRA 55 thermal field emission scanning electron microscope (SEM) equipped with energy dispersive X-ray spectroscopy (EDS) and confocal laser scanning microscope (CLSM, OLYMPUSOLS4100). The SEM images were processed to acquire the area fraction of DRXed grains by image-pro Plus 6 software. The phase composition of the studied alloys was detected using a D8 Advance X-ray diffraction with a Cu target. The scanning angel was 20° to 90° and the scanning speed was 6°/min.

2 Results and Discussion

2.1 Initial microstructure

The initial microstructures of solution-treated alloys before compression are shown in Fig. 1. The grain size of solution-treated AZ31 alloy varies roughly between 100 and 200 μm, with an average close to 148 μm. After the addition of 0.2wt% Ca, the coarse grains are slightly refined (about 96 μm) and the amount of homogeneous precipitates marginally increases. The SEM micrographs show that the alloys are composed of α-Mg matrix and some tiny and bright particles, especially AZ31-0.2Ca alloy. The EDS results of point 1 Fig. 1b are shown in Fig. 1c. According to the EDS result, the contents of Al and Ca are 40.33at% and 18.98at%, and only 0.12at% Mn and 0.39at% Zn are detected. In addition, the mole ratio of n(Al): n(Ca) is close to 2: 1, indicating that the chemical composition of precipitates is Al_2Ca[13], and it can be demonstrated by the XRD result.

Fig. 2 shows the XRD patterns of AZ31 and AZ31-0.2Ca alloys. As seen in Fig. 2, AZ31-0.2Ca alloy is mainly composed of α-Mg matrix and Al_2Ca phase, and almost no other precipitates are detected. The reason is that the amounts of Al-Mn phase in AZ31 and AZ31-0.2Ca alloys are very small, and it is difficult for XRD to identify. In addition, α-Mg has a variety of textures with different intensities, indicating that the studied alloys exhibit random texture. Obviously, the intensities of (0002) α-Mg peaks of solution-treated AZ31,

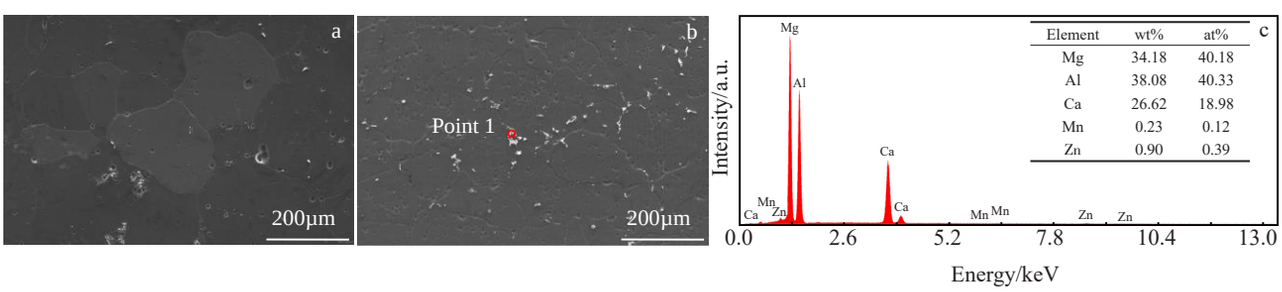


Fig.1 Initial microstructures of solution-treated AZ31 (a) and AZ31-0.2Ca alloys (b); (c) EDS results of point 1 in Fig.1b

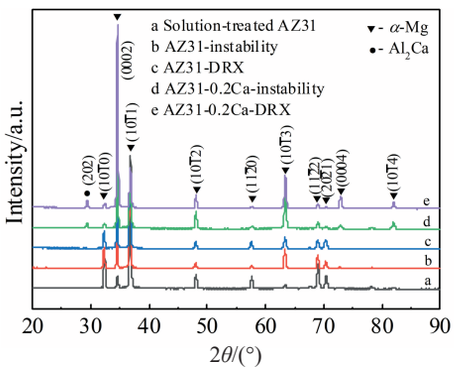


Fig.2 XRD patterns of solution-treated AZ31 and AZ31-0.2Ca alloys

AZ31-instability, AZ31-DRX, AZ31-0.2Ca-instability and AZ31-0.2Ca-DRX gradually increase, and the intensities of (10$\bar{1}$0) α-Mg peaks progressively decrease, which will be further discussed in Section 2.4.

2.2 Hot deformation behavior

The stress-strain curves of the studied alloys are shown in Fig. 3. It can be seen that the curves exhibit typical DRX softening characteristics at low temperature and high strain rate. That is, the flow stress gradually increases with strain up to a peak, and then decreases slowly to a final steady state value, during which DRX is the main dynamic softening mechanism. While the flow stress initially increases with increasing the strain slowly, up to a maximum, beyond which the flow stress keeps steady state at high temperature and low strain rate, i.e., DRV is the main softening behavior. Note that the position of the maximum stress is shifted to the lower strains with increasing the temperature, but strain rate has minor effect on it. This is attributed to the fact that processing at low temperature promotes deformation twinning, reflecting the competition between non-basal slip and twinning. Compared with twinning, the critical resolved shear stress of the non-basal slip is lower at high temperature[14]. Even though lower imposed strain is sufficient to meet necessary stress for basal and non-basal slip systems. It is noteworthy that the flow stress can be increased in the case of Ca-addition during hot deformation, as well as the work softening stage which is more gradual (Fig. 3). The reason is that the imposed strain cannot be accommodated because of inhibiting of the growth of recrystallized grains or the progress of twins by Al_2Ca precipitates in AZ31-0.2Ca alloy, and an additional hardening effect is provided[15].

Based on the dynamic material model (DMM) proposed by Prasad[16], processing maps of the studied alloys are shown in Fig.4. The gray zone represents instability parameter less than zero ($\xi(\dot{\varepsilon})\leq 0$), which is defined as instability region. The figures of these maps represent efficiency of power dissipation (η) and the condition for DRX to occur is η over 0.3[17], so the blue zone with η over 0.3 is defined as DRX domain. Obviously, minor Ca element significantly reduces instability

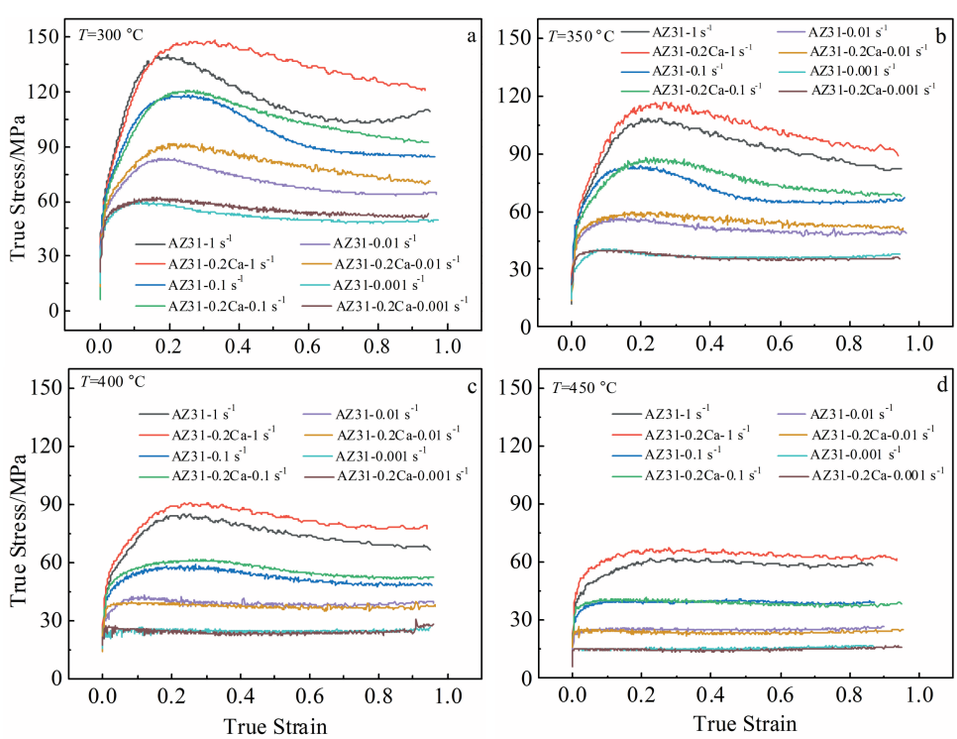


Fig.3 True stress-strain curves of solution-treated AZ31 and AZ31-0.2Ca alloys compressed at strain rate of 0.001~1 s^{-1} and temperatures of 300 °C (a), 350 °C (b), 400 °C (c), and 450 °C (d)

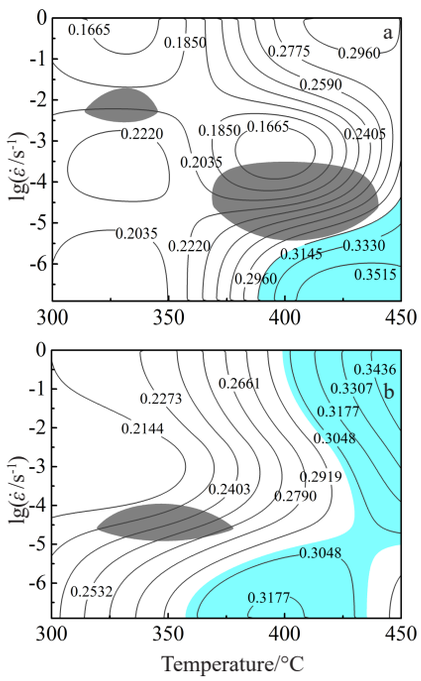


Fig.4 Processing maps of solution-treated AZ31 (a) and AZ31-0.2Ca alloy (b) with the strain of 0.92 (gray represents instability region ($\xi(\dot{\varepsilon})\leq 0$), blue shows possible DRX domain ($\eta > 0.3$))

zone and enlarges DRX domain, indicating that Ca-addition is favorable to recrystallization and enhances hot workability of solution-treated AZ31 alloy. Note that the efficiency of power dissipation (η) of AZ31-0.2Ca alloy is remarkably enlarged compared with that of AZ31 alloy at the same strain. Moreover, the area fraction of DRX ($\eta > 0.3$) of AZ31-0.2Ca alloy is higher than that of AZ31 alloy, which is ascribed to hindering of the movement of grain boundaries and increase of the number of grain nucleation sites by Al_2Ca precipitates in the Ca-addition alloy[18]. Fig. 5 shows the typical microstructure of the studied alloys with different efficiency of power dissipation. The instability zone exhibits heterogeneous microstructure, consists of large coarse grains surrounded by fine equiaxed ones due to partial DRX, dispersing like necklaces. Moreover, obvious wedge cracks are visible in the DRXed grains along coarse grains in instability region (Fig.5c), which is due to the flow localization bands caused by stress concentration in the coarse grain area[19]. Obviously, the DRX volume fraction of AZ31-0.2Ca alloy in the instability region is about 42.8% and much higher than that of AZ31 alloy (32.5%), which is in good agreement with the results of processing maps (Fig. 4). The DRX domain experiences relatively complete dynamic recrystallization, exhibiting a homogeneous fine grain microstructure, which is because a higher temperature (400 ℃) exhibits greater nucleation driving force and a lower strain rate (0.001 s^{-1}) provides enough time for nucleating[9]. Therefore, the sample obtained at 400 ℃/0.001 s^{-1} by hot deformation has superior hot workability due to η over 0.3 and homogenous fine grain microstructure.

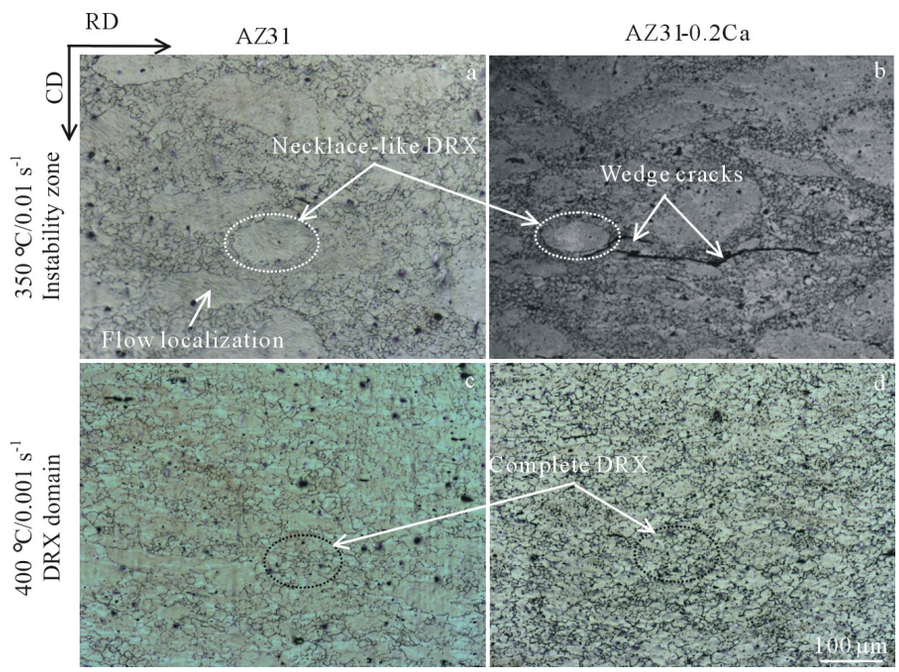


Fig.5 Microstructures of AZ31 (a, b) and AZ31-0.2Ca (c, d) alloys during hot deformation (RD and CD stand for radial and compression directions, respectively)

2.3 Corrosion behavior

2.3.1 Electrochemical test

According to processing maps (Fig.4), the instability region (350 ℃/0.01 s^{-1}) and DRX domain with high efficiency of power dissipation (400 ℃/0.001 s^{-1}) are selected for corrosion test, and the meaning of the sample abbreviation is shown in Table 2.

Fig. 6a shows the polarization curves of various samples, and the fitting results are summarized in Table 3. Obviously, the anode branches of investigated alloys exhibit obvious passivation phenomenon. The corrosion current densities (J_{corr}) of solution-treated AZ31, AZ31-instability, AZ31-DRX, AZ31-0.2Ca-instability and AZ31-0.2Ca-DRX are 1.9315, 0.1435, 0.1308, 0.1259 and 0.1153 mA·cm^{-2}, respectively, which gradually decrease, indicating that the corrosion resistance is gradually improved and it will be further discussed in Section 2.4. But the corrosion potentials of the studied alloys are -1.47, -1.43, -1.49, -1.49 and -1.40 V, which do not gradually increase; it slightly deviates from the results of corrosion current density. It is likely that the corrosion potentials fluctuate due to the instability of the corrosion system caused by the change of pH value of solution. Corrosion potential is the thermodynamic parameter of corrosion, which just indicates the corrosion tendency. While corrosion current density is the kinetic parameter, which directly relates to the corrosion rate[20]. Fig. 6b~6d illustrate the Nyquist and Bode plots of AZ31-*x*Ca alloys obtained by EIS measurement. The Nyquist plots all exhibit a small capacitive loop in the high frequency, a large capacitive loop in the middle frequency and a low-frequency inductive loop.

Table 2 Meaning of the following abbreviations

Deformation conditions	AZ31	AZ31-0.2Ca
350 ℃/0.01 s^{-1}	AZ31-instability	AZ31-0.2Ca-instability
400 ℃/0.001 s^{-1}	AZ31-DRX	AZ31-0.2Ca-DRX

To further elucidate the corrosion behavior of the five alloys, the equivalent circuit is shown in Fig. 6e and the corresponding fitting results are summarized in Table 3. The polarization resistance (R_p) can be obtained by Eq. (1)[21]. In general, charge transfer resistance (R_{ct}) is related to the capacitance loop at the high frequency, which can be used to describe corrosion resistance. Film resistance (R_f) value, related to the capacitance loop at the middle frequency, indicates the protective ability of the corrosion product film[22] and low frequency inductive impedance (R_L) is related to the corrosion nucleation at the initiation stage of localized corrosion[23]. Furthermore, a lower value of CPE represents smaller corrosion reaction area and a lower value of CPE_{dl} implies a thicker and more compact film on the sample surface[24]. It can be seen that the DRX domain of AZ31-0.2Ca alloy shows higher values of R_{ct} and R_f together with lower values of CPE and CPE_{dl}, indicating a lower metallic dissolution

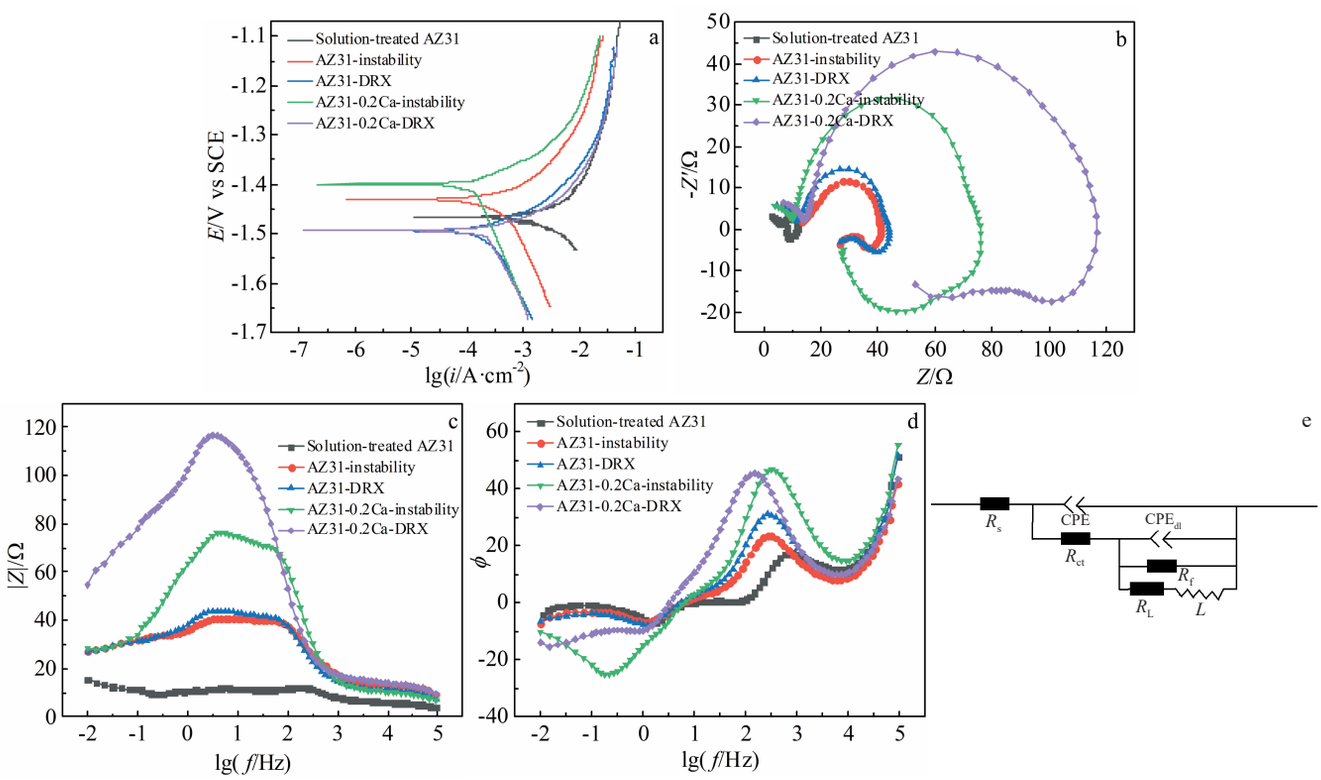


Fig.6 As-recorded polarization curves (a), Nyquist curves (b), corresponding Bode plot (c, d) and equivalent circuit (e) of AZ31 and AZ31-0.2Ca alloys in 3.5wt% NaCl solution

Table 3 Values of circuit elements in equivalent circuit

Parameters	Solution-treated AZ31	AZ31-instability	AZ31-DRX	AZ31-0.2Ca-instability	AZ31-0.2Ca-DRX
R_s/Ω·cm^2	0.01	0.58	0.01	0.98	0.01
CPE/×10^{-6} F·cm^{-2}	0.32	2.89	0.40	33.65	0.88
n	1.00	0.91	0.95	0.91	0.85
R_{co}/Ω·cm^2	5.70	11.62	13.53	14.21	15.17
CPE_{dl}/×10^{-6} F·cm^{-2}	469.40	54.34	53.02	50.12	47.73
n_{dl}	0.73	0.91	0.92	0.71	0.93
R_{ct}/Ω·cm^2	10.86	26.68	31.80	65.36	96.74
R_L/Ω·cm^2	11.68	47.09	47.55	26.15	112.80
L/H·cm^2	0.01	13.58	16.18	33.60	110.00
R_p/Ω·cm^{-2}	14.69	36.00	42.33	74.57	110.11

rate and a more protective passivation film. The R_p values of solution-treated AZ31, AZ31-instability, AZ31-DRX, AZ31-0.2Ca-instability and AZ31-0.2Ca-DRX are 14.69, 36.00, 42.33, 74.57 and 110.11 Ω·cm^2, respectively, which gradually increase, indicating that the corrosion resistance of the five samples sequentially increases. Obviously, the R_p value of DRX domain of AZ31-0.2Ca alloy is the largest among all of them and it has the best corrosion resistance due to homogeneous fine grain microstructure. The corrosion rates (C_w) acquired by immersion mass loss method are shown in Fig.7 and Table 4. Obviously, the corrosion rates (P_i) of DRX domain of AZ31 and AZ31-0.2Ca alloys are 47.71 and 7.37 mm/a, respectively, which are much lower than that of the instability region (51.04 and 10.25 mm/a), revealing that the heterogeneous microstructure and wedge cracks are harmful to the corrosion resistance of AZ31 alloy.

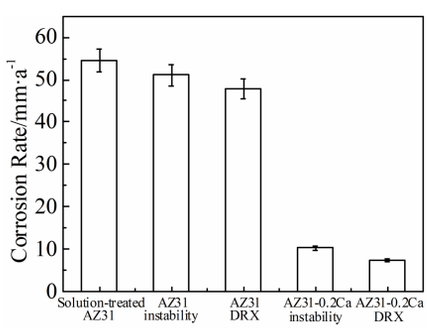


Fig.7 Corrosion rates of AZ31 and AZ31-0.2Ca alloys immersed in 3.5wt% NaCl solution for 5 d

Table 4 Electrochemical parameters obtained from potentiodynamic polarization testing and corrosion rates calculated from mass loss measurement

Specimens	E_{corr}/V	J_{corr}/mA·cm^{-2}	C_w/mm·a^{-1}
Solution-treated AZ31	-1.47	1.9315	54.46
AZ31-instability	-1.43	0.1435	51.04
AZ31-DRX	-1.49	0.1308	47.71
AZ31-0.2Ca-instability	-1.49	0.1259	10.25
AZ31-0.2Ca-DRX	-1.40	0.1153	7.37

$$R_p=R_{ct}+\frac{1}{\frac{1}{R_L}+\frac{1}{R_f}} \quad (1)$$

2.3.2 Hydrogen evolution test

Fig.8 presents the hydrogen evolution curves for AZ31 and AZ31-0.2Ca alloys immersed in 3.5wt% NaCl solution. The curves of AZ31 alloy can be divided into two stages accompanied by the corresponding dashed line (Fig. 8a and 8b). During the first 0~1 h immersion time, the hydrogen evolution rates increase rapidly. From 1 h to 24 h, the corrosion rates turn to relatively low positive shift rates, which is mainly because the samples are passivated owing to the accumulation of the corrosion products on the surface of the samples with increasing the immersion time (Fig. 6a). As shown in Fig. 8c and Fig. 8d, the curves of AZ31-0.2Ca alloy can be divided into three stages. The corrosion rates increase rapidly at the first 0~2 h immersion time and then decrease significantly, which is attributed to the formation of a more compact, stable corrosion products film and will be discussed further in Section 2.4. From 20 h to 24 h, the hydrogen evolution rates remain relatively stable since the formation and exfoliation of the corrosion products reach a dynamic equilibrium. It should be noted that the corrosion rates of AZ31 alloy are 5~6 times larger than that of AZ31-0.2Ca alloy owing to a more resistant Ca-rich passivation layer than the Mg-rich passivation layer[25]. The hydrogen evolution rates of the DRX domain are slightly lower than that of the instability region due to homogeneous fine grain microstructure, which comes in line with the results obtained by electrochemical and immersion weightless tests. Combined with the previous analysis of Section 2.2, homogeneous fine grain microstructure by hot deformation at 400 ℃/0.001 s^{-1} of the studied alloys simultaneously perform good hot workability and superior corrosion resistance.

2.3.3 Corrosion morphology

To illustrate the corrosion morphology, SEM morphologies of the studied alloys with corrosion products are shown in Fig. 9. The corrosion product film of AZ31 alloy is loose,

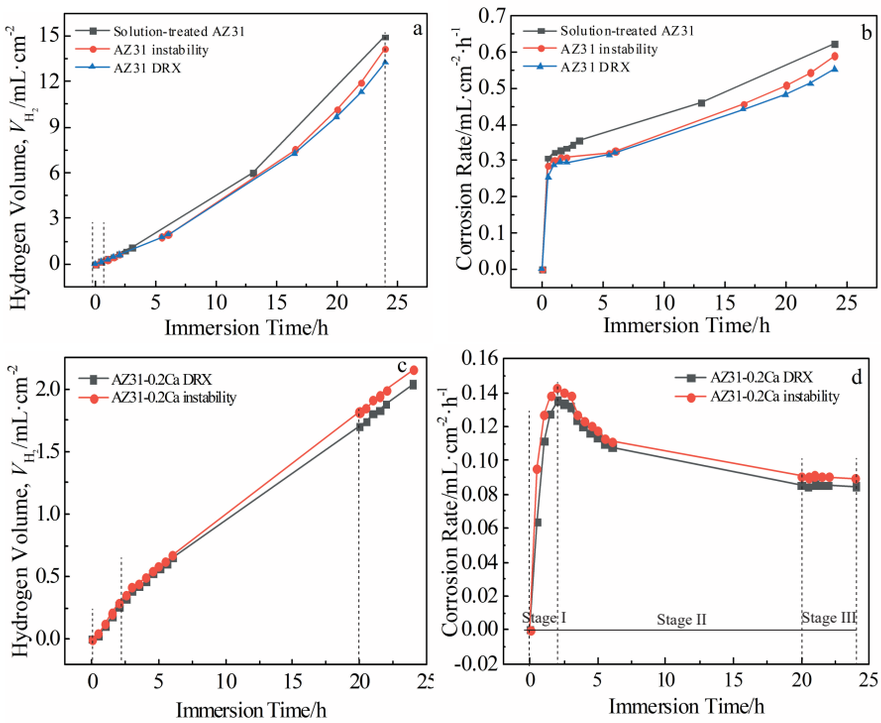


Fig.8 Hydrogen volume V_{H_2} evolution (a, c) and corrosion rates (b, d) of alloys after immersion for 24 h in 3.5wt% NaCl solution

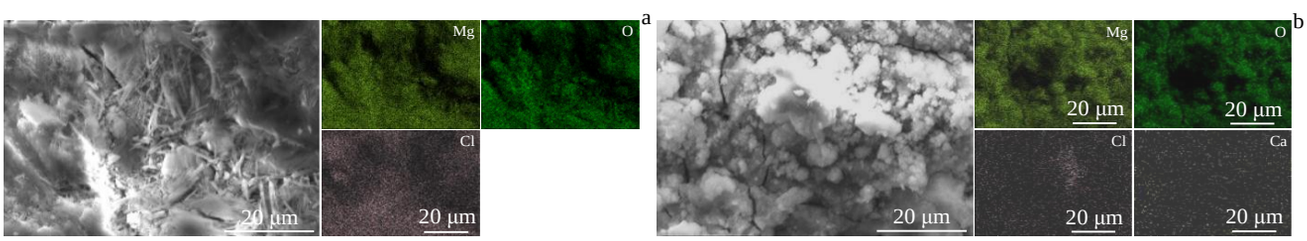


Fig.9 Corrosion products of AZ31 (a) and AZ31-0.2Ca alloys (b) immersed in 3.5wt% NaCl solution for 5 d

rough and has many cracks, and even peels off from the substrate (Fig.9a). According to the EDS results, the corrosion products are mainly rich in Mg, O and Cl elements. But the corrosion products of AZ31-0.2Ca alloy are relatively compact, intact, and mainly rich in Mg, O, Cl and Ca elements (Fig. 9a). The Pilling-Bednorth ratio (PBR) and standard enthalpy of the compounds are shown in Table 5. The PBR values of MgO and CaO are less than one, which indicates that the tensile stress parallel to the oxide film is produced, eventually leading to micro-cracks[26]. Note that the PBR values of $Mg(OH)_2$ and $Ca(OH)_2$ are between one and two, implying that the oxide film is continuous and compact, and the lower enthalpy values of $Ca(OH)_2$ indicate greater chemical stability[26]. That is to say, the oxide film of AZ31-0.2Ca alloy is more compact, stable and protective due to the doping of a trace amount of $Ca(OH)_2$.

Table 5 PBR and standard enthalpy of related compounds[26]

Compounds	MgO	$Mg(OH)_2$	CaO	$Ca(OH)_2$	$CaCO_3$
PBR	0.80	1.80	0.64	1.30	1.43
Enthalpy/ kJ·mol^{-1}	-601.7	-924.66	-635.1	-986.1	-1206.9

2.4 Effect of microstructure on corrosion behavior

The DRX domain obtained at 400 °C/0.001 s^{-1} exhibits a homogeneous fine grain microstructure due to relatively complete dynamic recrystallization (Fig. 5b and 5d). Wu et al[27] concluded that small grains with more grain boundaries not only serve as corrosion barrier, but also provide more nucleation sites to passivation films. Luo et al indicated that the relationship between grain size and corrosion resistance depends on whether the passivation occurs[28]. Obviously, the anode branches of investigated alloys exhibit obvious passivation phenomenon (Fig.6a), so the DRX domain with smaller grains performs a better corrosion resistance. According to the processing map (Fig.4) and homogeneous fine grain microstru-

cture (Fig. 5), the DRX domain with higher efficiency of power dissipation exhibits good hot workability. The instability region obtained at 350 ℃/0.01 s^{-1} exhibits heterogeneous microstructure due to partial DRX and obvious wedge cracks in the DRXed grains along coarse grains owing to flow localization bands (Fig.5b and 5d). Corrosion occurs primarily at surface crystalline defects (wedge cracks) due to the high energy caused by crystalline defects (wedge cracks)[28]. Moreover, wedge cracks can serve as channels for ion diffusion, allowing aggressive Cl^- ions to penetrate the substrate and to accelerate further corrosion of fresh Mg matrix [9,29]. Therefore, the instability region performs worse corrosion resistance than DRX domain. DRX domain with higher efficiency of power dissipation and homogeneous fine grain microstructure by hot deformation at 400 ℃/0.001 s^{-1} simultaneously performs good hot workability and superior corrosion resistance.

After adding 0.2wt% Ca element, grain size decreases from 136 μm to 87 μm and uniformly distributed Al_2Ca precipitates appear (Fig. 1). As shown in Fig. 4, minor Ca element can obviously reduce the instability zone and enlarge the DRX domain. Moreover, the DRX volume fraction of AZ31-0.2Ca alloy is much higher than that of AZ31 alloy (Fig. 5), which indicates that Ca element can improve the hot workability by facilitating recrystallization and grain refinement. The corrosion products of AZ31-0.2Ca alloy are relatively more compact, intact and protective by doping a trace mount of $Ca(OH)_2$, which is confirmed in Fig.9. Research indicated that fine grains and uniformly distributed precipitates decrease galvanic corrosion intensity by forming denser corrosion film layer to enhance corrosion resistance[6,30]. Consequently, minor Ca addition can significantly improve the hot workability and corrosion resistance of solution-treated AZ31 alloy. Combined with previous analysis, therefore, the corrosion rate presents the order of solution-treated AZ31>AZ31-instability>AZ31-DRX>AZ31-0.2Ca-instability>AZ31-0.2Ca-DRX.

What's more, in Fig. 2, the intensities of (0002) α-Mg peaks of solution-treat AZ31, AZ31-instability, AZ31-DRX, AZ31-0.2Ca-instability and AZ31-0.2Ca-DRX gradually increase, and the intensities of $(10\bar{1}0)$ peaks progressively decrease. As a result, AZ31-0.2Ca-DRX exhibits the highest basal texture and the lowest non-basal texture. The intensity of basal texture is consistent with the volume fraction of recrystallized grains, which confirms that the newly generated recrystallized grains are almost basal texture. The different crystal planes have great influence on the corrosion resistance of AZ31 alloy because of the different surface energy[31-33]. The surface energy for Mg $(10\bar{1}0)$ and (0001) is 30.4 and 15.4 kJ/mol, respectively, and it gradually decreases. The loosely packed plane has a higher surface energy and a lower activation energy for dissolution in comparison with the closely packed crystal plane[34]. That is to say, the basal texture has better corrosion resistance than non-basal texture. Therefore, AZ31-0.2Ca-DRX with the highest basal texture exhibits the best corrosion resistance, while solution-treated AZ31 alloy with the highest non-basal texture shows the worst corrosion resistance, which is completely in line with the previous experiment results. Consequently, the DRX domain with high efficiency of power dissipation and basal texture of AZ31-0.2Ca alloy performs good hot workability and superior corrosion resistance.

3 Conclusions

1) Minor Ca-addition can significantly improve the hot workability and corrosion resistance of AZ31 alloy due to grain refinement by facilitating recrystallization and formation of a more compact, stable and protective corrosion product layer doped with minor $Ca(OH)_2$.

2) The instability region performs worse corrosion resistance than DRX domain due to obvious wedge cracks and heterogeneous microstructure. Moreover, the wedge cracks caused by flow localization band can serve as channels for the diffusion of aggressive Cl^- and accelerate further corrosion of Mg matrix .

3) The DRX domain with high efficiency of power dissipation and homogeneous fine grain structure by hot deformation at 400 ℃/0.001 s^{-1} of AZ31-0.2Ca alloy simultaneously performs good hot workability and superior corrosion resistance.

References

1 Li D, Wang H, Luo D *et al*. *Surface and Coatings Technology*[J], 2018: 347

2 Liu D, Guo C, Chai L *et al*. *Materials Science and Engineering B* [J],2015,195(5): 50

3 Zhou M R, Huang X S, Morisada Y *et al*. *Materials Science and Engineering A*[J], 2020, 769: 138 474

4 Chaudry U M, Hamad K. *Materials Letters*[J], 2018

5 Zhang B, Wang Y, Geng L *et al*. *Materials Science & Engineering A*[J], 2012, 539: 56

6 Ralston K D, Birbilis N, Davies C H J. *Scripta Materialia*[J], 2010, 63(12): 1201

7 Mingo B, Arrabal R, Mohedano M *et al*. *Materials & Design*[J], 2017, 130: 48

8 Sun Y, Wang R, Peng C *et al*. *Materials Characterization*[J], 2020, 159: 110 031

9 Tsao L C, Chen C H, Wu R W *et al*. *Journal of Manufacturing Processes*[J], 2015, 18: 167

10 Kaviani M, Ebrahimi G R, Ezatpour H R. *Materials Chemistry and Physics*[J], 2019, 234: 245

11 Cheng W, Bai Y, Ma S *et al*. *Journal of Materials Science & Technology*[J], 2019

12 Wang C, Liu Y, Lin T *et al*. *Materials Characterization*[J], 2019, 157: 109 896

13 Zhang C, Wu L, Huang G *et al*. *Journal of Alloys and Compounds*[J], 2020, 823: 153 844

14 Oh-Ishi K, Mendis C L, Homma T *et al*. *Acta Materialia*[J], 2009, 57(18): 5593

15 Wu H Y, Yang J C, Zhu F J *et al*. *Materials Science & Engineering A*[J], 2012, 550: 273

16 Chen X R, Liao Q Y, Niu Y X *et al*. *Journal of Alloys and Compounds*[J], 2019, 803: 585
17 Liu L, Ding H. *Journal of Alloys and Compounds*[J], 2009, 484(1-2): 949
18 Yang J, Peng J, Nyberg E A *et al*. *Applied Surface Science*[J], 2016, 369: 92
19 Hadadzadeh A, Wells M A, Shaha S K *et al*. *Journal of Alloys and Compounds*[J], 2017, 702: 274
20 Chunan Cao. *Principles of Electrochemistry of Corrosion*[M]. Beijing: Chemical Industry Press, 2008
21 King A D, Birbilis N, Scully J R. *Electrochimica Acta*[J], 2014, 121: 394
22 Jeong Y S, Kim W J. *Corrosion Science*[J], 2014, 82(5): 392
23 Zhang Y, Li J, Li J. *Journal of the Mechanical Behavior of Biomedical Materials*[J], 2018, 80: 246
24 Bahmani A, Arthanari S, Shin K S. *Journal of Magnesium and Alloys*[J], 2019, 7: 38
25 Metalnikov P, Ben-Hamu G, Eliezer D *et al*. *Journal of Alloys and Compounds*[J], 2019, 777: 835
26 Zeng R C, Sun L, Zheng Y F *et al*. *Corrosion Science*[J], 2014, 79(2): 69
27 Wu P P, Xu F J, Deng K K *et al*. *Corrosion science*[J], 2017, 127(10): 280
28 Luo Y, Deng Y, Guan L *et al*. *Corrosion Science*[J], 2019, 167: 108 338
29 Sun Y, Wang R, Peng C *et al*. *Corrosion Science*[J], 2020, 167: 108 487
30 Birbilis, N, Ralston *et al*. *Corrosion Engineering&Science and Technology*[J], 2010: 45(3): 224
31 Song G L, Xu Z. *Corrosion Science*[J], 2012, 63(10): 100
32 Pawar S, Slater T J A, Burnett T L *et al*. *Acta Materialia*[J], 2017, 133: 90
33 Jia H, Feng X, Yang Y. *Journal of Materials Science & Technology*[J], 2018, 34: 1229
34 Song G L, Mishra R, Xu Z Q. *Electrochemistry Communications* [J], 2010, 12(8): 1009

热变形提高Mg-3Al-1Zn-0.1Mn-0.2Ca合金的热加工性和耐蚀性

王盼盼，江海涛，王玉娇，张　韵，于博文，曹志明，仲彬彬
(北京科技大学 工程技术研究院，北京 100086)

摘　要：研究了功率耗散系数对AZ31合金热加工性和腐蚀行为的影响。结果表明：微量的Ca元素可以促进动态再结晶（DRX）而细化晶粒和形成掺杂微量$Ca(OH)_2$更具保护性的腐蚀产物层从而提高合金热加工性和耐蚀性。失稳区由于不均匀的组织和明显的楔形裂纹耐蚀性差于DRX区域。而且流动局部带造成的楔形裂纹为侵蚀性Cl^-的扩散提供了通道并加速了镁基体的进一步腐蚀。Mg-Al-Zn-Mn-Ca合金在400 ℃/0.001 s^{-1}热压缩得到大功率耗散系数和均匀细小组织的DRX区域同时具有优异的热加工性和耐蚀性。

关键词：AZ31合金；微观组织演变；耐蚀性；热加工性

作者简介：王盼盼，女，1996年生，硕士，北京科技大学工程技术研究院，北京 100086，电话：010-62332598，E-mail：wpp1424440771@126.com